Millán-Merino, A., Fernández-Tarrazo, E. & Sánchez-Sanz, M. (2021). Numerical analysis of the autoignition of isolated wet ethanol droplets immersed in a hot and humid air atmosphere. *Combustion and Flame, 226*, 42–52.

DOI: 10.1016/j.combustflame.2020.11.023

Numerical analysis of the autoignition of isolated wet ethanol droplets immersed in a hot and humid air atmosphere

Alejandro Millán-Merino[a], Eduardo Fernández-Tarrazo[a], Mario Sánchez-Sanz[a]

[a]*Dept. Ingeniería Térmica y de Fluidos, Universidad Carlos III de Madrid, Leganés 28911, Spain*

Abstract

Results of time-dependent, spherically symmetrical computations of the vaporization and combustion of ethanol and ethanol/water droplets are reported. Mixture-average transport was employed, along with a systematically reduced chemical-kinetic mechanism involving 15 overall steps among 17 chemical species, to speed the computations by a factor of about 100 over what would be required if full detailed chemistry had been used. Absorption of water from the gas surrounding the droplet and its diffusive transport within the liquid phase were taken into account, providing excellent agreement with previous experimental and computational results for the combustion of ethanol droplets in air. On the other hand, the assumption of rapid liquid-phase mixing produced very poor agreement when water condensation on the droplet surface or hydrous ethanol are considered. To characterize autoignition, we define the critical autoignition temperature T_∞^c as the critical ambient temperature below which autoignition is not observed. Computations for autoignition of cold ethanol/water droplets in air showed that T_∞^c decreases with increasing initial droplet diameters. In the range of parameters under consideration, ignition was found to take place always before complete vaporization of the droplet, and the ignition time was found to become longer with the increasing initial water content of the liquid ethanol droplet. On the contrary, addition of water vapor to the initial air atmosphere was found to shorten the ignition time, increasing ethanol vaporization rate as a consequence of the extra heat release associated with water absorption into the liquid.

Keywords: ethanol droplet combustion, humidity, reduced chemistry, auto-ignition

1. Introduction

Liquid fuels are convenient in combustion-based transport and industry applications because of their availability, high energy density and easy storage in atmospheric conditions [1]. To release their chemical energy in combustion applications they must first be vaporized in an endothermic phase change that takes place after injecting the fuel, typically as a spray,

directly in the combustion chamber. The relevance of the problem has motivated an intensive research in both liquid fuel vaporization and combustion for sprays [2–5] and individual droplets [6–9]. To ameliorate air quality in big cities, CO_2 and diesel-specific engine pollutants emissions are in the spotlight, especially particulates and nitrogen oxide NOx. The most popular strategy to reduce NOx makes use of aftertreatment technologies such as the selective catalytic reduction [10] and the injection of ammonia or urea [11] in the exhaust gases to reduce NOx into harmless nitrogen. On the other hand, the strategy to reduce greenhouse gas emissions is based on a sharp increase of the engine efficiency and in the substitution of oil and diesel by other fuels with better carbon footprint, such as ethanol, that can be added in significant amounts to existing fuels. Additionally, the utilization of ethanol/gasoline blends in spark ignition engines increases the octane index allowing larger compression ratios that lead to better efficiencies [12]. The use of mixtures of ethanol/diesel and ethanol/biodiesel is seen as a good strategy to reduce soot, promote the vaporization of biodiesel droplets [13] and increase the flexibility in the control of NOx emissions [14].

The transient behaviour of the autoignition of alkane droplets has been extensively studied due to its technological interest. Both experimental [15–20] and numerical studies [21–23] of n-heptane, n-dodecane and n-hexadecane have revealed a catalog of exotic ignition behaviours, that includes single-stage ignition, two-stage ignition and cool flames.

Unlike the hydrophobic alkanes, in the vaporization and combustion of alcohols, water vapor freely condensates on the surface of the droplet and subsequently dissolves into the droplet interior [24], forming a multicomponent droplet whose vaporization differs from the characteristic d^2-law. The difficulties to control the ambient conditions [25] explains the lack of experimental and numerical studies on the evaporation and autoignition of ethanol droplets. The experimental [13, 24, 26–30] and numerical [31, 32] studies found in the literature focused, mainly, in the quasi-steady regime, when the flame temperature remains almost constant and the droplet radius recedes following the d^2-law. In this case, the experimental setup is simpler and the time available for observation is maximized by forcing ignition early in the droplet lifetime. Also, from a numerical point of view, the stiffness of the problem is reduced. Only the numerical study by Kazakov et al. [31] takes into account the water accumulation in the liquid phase but they used, as initial condition, a gas phase temperature distribution that simulates the presence of a spark [33]. Unlike them, this work includes the gravityless description of the unsteady evaporation and autoignition stages of an individual droplet of radius $a(t)$ that precedes the quasi-steady regime in a hot air environment at a temperature T_∞ and a pressure p_∞, giving an accurate description of the sudden increase of temperature that characterizes this period and taking into account the water content of liquid ethanol and water condensation either from the ambience or generated at the flame.

To model autoignition, we use a reduced combustion mechanism [34], formed by 15 reactions and 17 species [35], available at [36], to compute a complex unsteady combustion problem that involves autoignition, rich and lean flames and, finally, a quasi-steady diffusion flame located far from the liquid droplet surface.

2. Formulation

We will consider here the case of a single droplet with initial diameter of $d_0 = 2a_0$ in an infinite stagnant ambient without gravity or forced flow as shown in the sketch in Fig. B.1. In these conditions, the flow has spherical symmetry provided that the initial conditions satisfy this property. The transient, spherically symmetric problem of droplet evaporation and combustion in microgravity conditions is mathematically described by the mass, species and energy conservation equations,

$$\frac{\partial \rho_\beta}{\partial t} + \frac{1}{r^2}\frac{\partial}{\partial r}(r^2 \rho_\beta u_\beta) = 0, \tag{1}$$

$$\frac{\partial (\rho_\beta Y_{\beta,i})}{\partial t} + \frac{1}{r^2}\frac{\partial}{\partial r}(r^2 \rho_\beta Y_{\beta,i} u_\beta) = -\frac{1}{r^2}\frac{\partial}{\partial r}(r^2 J_{\beta,i}) + \omega_{\beta,i}, \quad i = 2, ..., N_\beta, \tag{2}$$

$$\frac{\partial (\rho_\beta h_\beta)}{\partial t} + \frac{1}{r^2}\frac{\partial}{\partial r}(r^2 \rho_\beta h_\beta u_\beta) = -\frac{1}{r^2}\frac{\partial}{\partial r}(r^2 q_\beta) + Q_\beta, \tag{3}$$

with ρ_β, u_β and h_β the density, the velocity and thermal enthalpy of the mixture, respectively. The sub-index i represents the ith species in both the liquid phase $\beta = \ell$ inside the droplet and the gas phase $\beta = \mathrm{g}$. $Y_{\beta,i}$ is the mass fraction and $Q_\beta = -\sum_{i=1}^{N_\beta} h^{\mathrm{ref}}_{\beta,i}\omega_{\beta,i}$ the heat released, with $h^{\mathrm{ref}}_{\beta,i}$ the enthalpy at the reference temperature $T^{\mathrm{ref}} = 298.15$ K and $\omega_{g,i}$ the mass production or consumption rate calculated using the 15-steps reduced combustion mechanism derived by Millán-Merino et al [37] as a correction to the 14-steps combustion mechanism given in [34]. Heat production in the liquid phase is neglected and $\omega_{l,i} = 0$.
The species mass flux term for the gas phase in equation (2) is calculated with the mixture averaged model [38] with conservative flux correction [39]

$$J_{\mathrm{g},i} = -\rho_{\mathrm{g}} Y_{\mathrm{g},i}\left(V^0_{d,i} + V^c_d\right), \tag{4}$$

where $V^0_{d,i} = -(D_{\mathrm{g},i}/X_{\mathrm{g},i})(\partial X_{\mathrm{g},i}/\partial r)$, $V^c_d = -\sum_{i=1}^{N_{\mathrm{g}}} Y_{\mathrm{g},i} V^0_{d,i}$,
$X_{\beta,i}$ is the mole fraction and $D_{\mathrm{g},i} = (1 - Y_{\mathrm{g},i})/(\sum_{j\neq i}^{N_{\mathrm{g}}} X_{\mathrm{g},j}/D_{\mathrm{g},ji})$ is the mixture diffusion coefficient, with $D_{\mathrm{g},ij}$ the binary diffusion coefficient, for the pair of species i and j, obtained from the kinetic theory. For the liquid phase, the mass flux term is calculated using the Fick's law,

$$J_{\ell,i} = -\rho_\ell D_{\ell,i}\frac{\partial Y_{\ell,i}}{\partial r} \tag{5}$$

and the mixture diffusion coefficient is determined by the Wilke-Chang equation [40]

$$D_{\ell,i} = 1.173 \times 10^{-16} \frac{\sqrt{\sum_{j \neq i}^{N_\ell} X_{\ell,j} \varphi_j W_j} T}{\mu_\ell \mathrm{V}_{\ell,i}^{0.6}} \tag{6}$$

where W_i is the species mole mass, μ_ℓ the mixture viscosity, $\mathrm{V}_{\ell,i}$ the molar volume. The association factor takes the values $\varphi_i = 2.6$ for water and $\varphi_i = 1.5$ for ethanol. In equation (3), the thermal heat flux term q_β is obtained from the generalized Fourier's law,

$$q_\beta = -k_\beta \frac{\partial T}{\partial r} + \sum_{i=1}^{N_\beta} J_{\beta,i} h_{\beta,i}, \tag{7}$$

where k_β is the thermal conductivity of the β phase and N_β denotes the number of species on each phase. Soluble species exist in both phases ($i = 1, ..., N_\ell$) but non-soluble species only exists in the gas phase ($i = N_\ell + 1, ..., N_\mathrm{g}$). Only the solubility of liquid ethanol and water has been considered. The most abundant species in each phase, ($i = I$), is obtained as $Y_{\beta,I} = 1 - \sum_{i \neq I}^{N_\beta} Y_{\beta,i}$. Equations (1)-(7) are supplemented with the Equations of State (EoS) of the gas written in the quasi-isobaric approximation $p_\infty / \rho_\mathrm{g} = T R_\mathrm{g}$. The density of the mixture in the liquid phase is computed as in [41] using the expression $\rho_\ell = \left(\sum_{i=1}^{N_\ell} X_{\ell,i} \rho_{\ell,i}^{1/2} \right)^2$, in which the individual densities of liquid species are obtained by fitting the experimental data published by [42, 43] using the expression introduced by [44],

$$\log \rho_{\ell,i} = A_{\rho,i} \log(T) + \frac{B_{\rho,i}}{T} + \frac{C_{\rho,i}}{T^2} + D_{\rho,i} + E_{\rho,i} T + F_{\rho,i} T^2 \tag{8}$$

2.1. Constitutive relations

Both the liquid and gas phases are considered ideal mixtures with heat capacity and enthalpy calculated as $c_{p_\beta} = \sum^{N_\beta} Y_{\beta,i} c_{p_{\beta,i}}$ and $h_\beta = \sum^{N_\beta} Y_{\beta,i} h_{\beta,i}$, in terms of the heat capacity $c_{p_{\beta,i}}$ and thermal enthalpy $h_{\beta,i}$ of the species i in the phase β.

The thermodynamic properties $c_{p_{\beta,i}}$ and $h_{\beta,i}$ of pure species are obtained using the NASA polynomials, where the coefficients are obtained whenever possible, from the San Diego mechanism database [45]. Those species not available in the San Diego database were taken from Burcat's database [46].

The gas phase molecular transport coefficients $D_{\mathrm{g},ij}$ and $k_{\mathrm{g},i}$ are obtained using the expression derived directly from the kinetic theory [47] using the transport database of the San Diego mechanism [45], while k_g is obtained using standard mixture average formula [48],

$$k_\mathrm{g} = \frac{1}{2} \left(\sum_{i=1}^{N_\mathrm{g}} X_{\mathrm{g},i} k_{\mathrm{g},i} + \frac{1}{\sum_{i=1}^{N_\mathrm{g}} X_{\mathrm{g},i} / k_{\mathrm{g},i}} \right). \tag{9}$$

For the liquid phase, the mixture thermal conductivity k_ℓ was obtained from a generalization of Filippov's equation [49],

$$k_\ell = \sum_{i=1}^{N_\ell} Y_{\ell,i} \left(k_{\ell,i} - \sum_{j=i+1}^{N_\ell} K_{i,j} Y_{\ell,j} \left| k_{\ell,i} - k_{\ell,j} \right| \right) \tag{10}$$

where Filippov's constant is $K_{i,j} = 0.72$. The conductivity of the pure species is computed using the correlation [44],

$$\log k_{\ell,i} = A_{k,i} \log(T) + \frac{B_{k,i}}{T} + \frac{C_{k,i}}{T^2} + D_{k,i} + E_{k,i} T + F_{k,i} T^2, \tag{11}$$

in which the coefficients are obtained by fitting with the experimental data published in [42, 43]. The viscosity of the liquid mixture is evaluated using the Grunberg and Nissan equation [50]

$$\mu_\ell = \exp \left(\sum_{i=1}^{N_\ell} X_{\ell,i} \ln \mu_{\ell,i} \right) \tag{12}$$

where the viscosity of the pure species is obtained using an expression analogous to Eq. (11) for the experimental results of [42, 43].

2.2. Boundary conditions

Boundary conditions are required at the center of the droplet and in the far field,

$$r = 0 : \frac{\partial T_\ell}{\partial r} = \frac{\partial Y_{\ell,i}}{\partial r} = u_\ell = 0, \tag{13}$$

$$r \to \infty : T_\mathrm{g} - T_\infty = Y_{\mathrm{g},i} - Y_{\infty,i} = 0, \tag{14}$$

while the boundary conditions at the liquid-gas interface are obtained by imposing the conservation of species mass and energy in a control volume extending from $r = a(t) - \delta$ to $r = a(t) + \delta$ in the limit $\delta \to 0$, yielding

$$-\dot{m}''(Y_{\mathrm{g},i} - Y_{\ell,i})_{r=a} = -(J_{\mathrm{g},i} - J_{\ell,i})_{r=a}, \qquad i = 2, ..., N_\ell, \tag{15}$$

$$-\dot{m}''(Y_{\mathrm{g},i})_{r=a} = -(J_{\mathrm{g},i})_{r=a}, \qquad i = N_\ell + 2, ..., N_\mathrm{g}, \tag{16}$$

$$-\dot{m}'' \sum_{i=1}^{N_l} \Big(Y_{\ell,i} \mathrm{L}_i(T) \Big)_{r=a} = \left(k_\mathrm{g} \frac{\partial T}{\partial r} - k_\ell \frac{\partial T}{\partial r} \right)_{r=a} - \sum_{i=1}^{N_l} \Big(J_{\ell,i} \mathrm{L}_i(T) \Big)_{r=a}, \tag{17}$$

where $a(t)$ is the instantaneous time-dependent radius of the droplet at a generic time t,

$$\dot{m}'' = -\rho_\ell (u_\ell - \dot{a})_{r=a} = -\rho_\mathrm{g} (u_\mathrm{g} - \dot{a})_{r=a} \tag{18}$$

is the mass vaporization rate per unit of surface area, T_s is droplet surface temperature respectively and $\dot{a} = da/dt$. The vaporization heat of each species is calculated as $\mathrm{L}_i(T) = h_{\mathrm{g},i}(T) - h_{\ell,i}(T) + \mathrm{L}_i^{\mathrm{ref}}$, with $\mathrm{L}_i^{\mathrm{ref}}$ representing the vaporization heat at the reference temperature.

Additionally, imposing the conservation of the chemical potential at the interface we obtain the Clausius equation [51],

$$(Y_{\mathrm{g},i})_{r=a} = \left(Y_{\ell,i}\frac{W_\ell}{W_\mathrm{g}}\right)_{r=a} \frac{p_{\mathrm{atm}}}{p_\infty}\gamma_i \exp\left(\int_{T_{\mathrm{b},i}}^{T_s} \frac{\mathrm{L}_i(T)}{R_{\mathrm{g},i}T^2}dT\right), \quad i = 1, ..., N_\ell, \tag{19}$$

where $T_{\mathrm{b},i}$ is the boiling temperature at atmospheric pressure ($p_{\mathrm{atm}} = 101325\mathrm{Pa}$), $R_{\mathrm{g},i}$ is the specific gas constant and γ_i the activity coefficient for the i species, obtained using the UNIFAC method [52].

2.3. Initial conditions

We will consider here the simplest case of a droplet with uniform composition and temperature that is placed at $t = 0$ in an infinitely large homogeneous gaseous ambient. Both temperature and fuel mass fraction profiles would then be discontinuous at the interface. In order to reduce the rigidity of such initial condition, the problem is integrated in time from $t = t_0$, using as initial condition the analytical solution obtained by Sazhin et al. [53] for an isolated non-evaporating droplet, to generate a smooth initial temperature profile

$$t = t_0 : \; T_\mathrm{g} = T_\infty + \frac{a_0}{r}(T_{d_0} - T_\infty)\mathrm{erfc}\left(\frac{r - a_0}{2\sqrt{D_{T,\mathrm{g},\infty}\; t_0}}\right), \tag{20}$$

valid for $t_0 \ll a_o^2/D_{T,\mathrm{g}}$, with $D_{T,\mathrm{g},\infty} = k_{\mathrm{g},\infty}/c_{p_{\mathrm{g},\infty}}\rho_{\mathrm{g},\infty}$ being the thermal diffusivity of the gas at infinity. The numerical parameter t_0 is as small as 10^{-5}s to minimize its influence on the posterior evolution of the problem, and sufficiently large to reduce the numerical stiffness of the problem. To avoid numerical problems, we imposed a smooth initial profile for the species mass fraction inspired by eq. (20) and defined as

$$t = t_0 : \; Y_{\mathrm{g},i} = Y_{\mathrm{g},i,\infty} + \frac{a_0}{r}(Y_{\mathrm{g},i,0} - Y_{\mathrm{g},i,\infty})\mathrm{erfc}\left(\frac{r - a_0}{2\sqrt{D_{T,\mathrm{g},\infty}\; t_0}}\right) \tag{21}$$

where the initial vaporized species profile at the droplet surface, $Y_{\mathrm{g},i,0}$, is a small quantity, of the order of 10^{-8}, that reduces the rigidity of the step-function initial condition but does not affect the solution.

To complete the set of initial condition, we assume that at $t = t_0$ the droplet, of uniform temperature and composition, is suddenly placed unperturbed in the gaseous ambient,

$$t = t_0 : \; Y_{\ell,i} - Y_{\ell,i,0} = T_\ell - T_{d_0} = 0; \quad i = 1, ..., N_\ell \tag{22}$$

A description of the numerical method and its validation is given in appendices A and B, respectively.

3. Droplet autoignition

The aim of this section is to compute numerically the autoignition time of an isolated droplet in an stagnant atmosphere describing the unsteady evaporation, autoignition and travelling premixed and diffusion flame stages that take place before achieving the quasi-steady combustion regime described in AppendixB. Droplet autoignition is a relatively slow phenomena that lasts up to 4.8 seconds in a 6 mm diameter droplet at 800 ºC. In the case of alcohol droplets in general, and ethanol in particular, water, either coming from the combustion products or from the ambient, condensates on the surface and dilutes inside the droplet. The technical difficulties to properly control ambient humidity conditions in a gravityless environment explain the lack of experimental measurements in the literature. Moreover, the accurate computational description of alcohol droplets autoignition requires of numerical codes capable of dealing with evaporation and combustion of multi-component ethanol/water droplets fitted to manage complex chemical reaction schemes accommodating sudden changes of temperature and composition in the reaction region. This has only recently been accomplished by [21, 23] for n-heptane, n-decane and n-dodecane droplets.
A spherical droplet burns as it is sketched in Fig. B.1, with a reaction zone located at $r = r_f >> a_0$ during the quasi-steady burning regime [54]. The heat conducted back from the flame to the droplet vaporizes the liquid fuel that reaches the reaction region by diffusion in a time of the order of $t_{\rm g} \sim a_0^2/D_{T,{\rm g}}$. After the droplet is introduced in a hot atmosphere at $t = t_0$, and before the flame is established, the droplet undergoes an unsteady period of pure evaporation in which the heat coming from the hot atmosphere vaporizes the fuel that diffuses out from the droplet surface forming a transient mixing diffusion layer of size $(D_{T,{\rm g}}t)^{1/2}$. Once the droplet radius a_0 and the ambient conditions are established (pressure, temperature and humidity), we define the ignition event as the instant of time $t_{\rm ig}$ at which the maximum gas temperature variation achieves its maximum value ${\rm d}T_{max}/{\rm d}t = {\rm d}T_{max}/{\rm d}t|_{\rm max}$ at a distance $r_{\rm ig} \sim a_0$ from the droplet center that will be obtained from the calculations.
The ignition time is compared throughout this section with the vaporization time, defined as the time needed to vaporize a droplet of initial radius a_0 with the heat conducted from the hot ambient. Its order of magnitude can be estimated from the balance between the vaporization flux at the droplet surface and the heat conducted from the gas phase to the liquid fuel during the quasi-steady stage defined in Eq. (17), yielding

$$t_{\rm evap} \sim \frac{\rho_\ell}{\rho_{\rm g}} \frac{a_0^2 {\rm L_b}}{D_{T,{\rm g}} c_{p_{\rm g}} (T_{\rm g} - T_{\rm b})} \tag{23}$$

The liquid density ρ_l and enthalpy of vaporization L_b are evaluated at the boiling temperature T_b. The gas thermal diffusivity $D_{T,g}$ is evaluated at mean gas temperature $T_m = (T_g + T_b)/2$. When combustion is present, and considering that the ignition time t_{ig} is much shorter than the vaporization time, the gas temperature T_g is defined as the adiabatic temperature $T_g = T_{ad}$. Crespo and Liñán [7] and Liñán and Williams [54] used the mixing time $t_g = a_0^2/D_{T,g}$ to define the non-dimensional time. Unlike them, we preferred the vaporization time to define $\tau = t/t_{evap}$, a characteristic time that is up to three orders of magnitude longer for large ambient temperatures.

The temperature and mass fraction of ethanol and oxygen at different stages of the autoignition process are depicted in Figs. B.2 and B.3. After placing the droplet in a hot and dry atmosphere $t > t_0$, the fuel starts vaporizing and mixing with the ambient air, generating a region where the equivalence ratio varies from rich conditions, close to the droplet, to lean conditions, far from the droplet. Since the concentration of fuel is low in the high temperature region, the formation of the ignition precursor H_2O_2 is slower than in homogeneous ignition systems [34]. When the H_2O_2 radical concentration reaches a level sufficiently high, near the instant denoted as $\tau = \tau_I$ in Figs. B.2 and B.3, its reactivity begins to produce an effect in the temperature and major species concentration fields. Shortly before the ignition event takes place, a lean premixed flame is generated, in the high temperature region, that propagates towards the droplet surface at $\tau = \tau_{II}$, gradually becoming a rich premixed flame as the flame front approaches the droplet surface ($\tau = \tau_{III}$). As the remaining oxygen between the moving flame front and the droplet surface is consumed, the premixed flame turns into an unsteady diffusion flame ($\tau = \tau_{IV}$) in which the flame moves outwards to approach its final quasi-steady propagation stage $r = r_f(\tau)$ as the droplet radius recedes ($\tau = \tau_V$).

The evolution with time of the main species profiles from the ignition point to quasi-steady solution is shown in detail in the animation included as supplementary material EtOHautoignitiontoQS.avi.

3.1. Critical autoignition temperature T_∞^c

In this section we computed the critical droplet autoignition temperature T_∞^c, defined as the ambient temperature below which $\tau_{ig} \to \infty$. In these conditions, a droplet with initial diameter d_0 completely evaporates before ignition. Figure B.4*a* shows the evolution of T_∞^c with the initial diameter for different droplet water contents and ambient humidities. To obtain the values of the critical temperature T_∞^c, we initiated the calculation procedure by setting a sufficiently large ambient temperature to ensure autoignition. As the ambient temperature is progressively reduced, the autoignition time becomes longer, to approach the vaporization time when the whole droplet vaporized without ignition at $T_\infty = T_\infty^c$. The variation of the autoignition time along the vertical and horizontal lines included in Figure

B.4a is depicted in Figures B.4b and B.4c. These subfigures clearly show the reverse effect of increasing the ambient temperature or initial droplet diameter on the autoignition time τ_{ig}, with the droplet vaporizing completely before autoignition for $T_\infty < 900$ K (Fig B.4b) and $d_0 < 0.1$ mm (Fig. B.4c). In the range of parameters considered, we found no ignition event occurs after complete vaporization of the droplet.

An example of this calculation process described above is depicted in Figs. B.5a and B.5c, where we plot the droplet diameter history and the maximum gas temperature for different ambient temperatures for an ethanol droplet with initial diameter $d_0 = 1$ mm. The temporal evolution of the maximum temperature T_{max} is plotted in Fig. B.5a for different ambient temperatures. This figure is used to determine the critical autoignition ambient temperature $T^c_\infty \simeq 900$ below which autoignition is not observed for a droplet with $d_0 = 1$ mm. Fig. B.5b elucidates how the autoignition time $\tau_{\rm ig}$ becomes longer as the temperature decreases, becoming infinity when the ambient temperature falls below the critical temperature $T_\infty = 900 < T^c_\infty$. Figure Fig. B.5$c$ illustrates how the autoignition event abruptly modifies the slope of the d^2-law that characterizes the evolution of the droplet radius with time, especially as the ambient temperature approaches its critical value.

Figure B.6 depicts the maximum gas temperature and normalized droplet surface as functions of time for small droplets of initial diameters $d_0 = 0.02$ and $d_0 = 0.05$mm, within the range of realistic droplet size in sprays applications. Notice that, for the 50 μm droplet, ignition occurs for $T_\infty = 1310$K to extinguish shortly after. On the contrary, the computations with sightlier lower ambient temperature $T_\infty = 1300$K did not show any increase of gas-phase temperature due to chemical reaction. This condition defines the critical autoignition temperature and separated both regimes. Our calculations showed that droplets with initial diameter below 20 μm induced a small temperature rise that that cannot be interpreted as an ignition event. As anticipated by Liñán [55], a quasi-steady solution cannot be achieved for such small droplets because the Damköhler number is below its critical value. Under these circumstances, we considered that proper autoignition does not take place for droplets with initial diameter $d_0 < 50$ μm and, therefore, they are not be included in the autoignition map depicted in Fig. B.4.

The time history of the ethanol vaporisation rate $\dot{m}_{\ell,\rm EtOH}$ is represented in Fig. B.7a for a droplet of initial diameter $d_0 = 1$ mm at ambient temperature slightly above the critical temperature $T_\infty = 910$ K$> T^c_\infty$. This figure illustrates how right after autoignition the computed vaporization rate sharply increases to rapidly decay once the flame moves away from the droplet surface reducing the heat flux to the liquid phase. In spite of the total absence of ambient moisture, Fig. B.7c illustrates how part of the water vapor that composes the combustion products condenses on the droplet surface right after ignition $\dot{m}_{l,\rm H_2O} < 0$,

mixing with ethanol before vaporizing again with the remaining liquid fuel $\dot{m}_{l,\mathrm{H_2O}} > 0$.

3.2. The effect of water content and ambient humidity

Figure B.8 represents the dependency of τ_{ig} on the initial volumetric droplet water content $\mathcal{V} = V_{\mathrm{H_2O}}/V_{\mathrm{droplet}}$ and on the ambient humidity

$$\mathcal{H} = \begin{cases} X_{\mathrm{g,H_2O},\infty}\dfrac{p_\infty}{p_{v,\mathrm{H_2O}}} & T_\infty < T_{\mathrm{b}} \\ X_{\mathrm{g,H_2O},\infty} & T_\infty > T_{\mathrm{b}} \end{cases} \tag{24}$$

here, we define $\mathcal{H}$ as the ambient relative humidity, when the ambient temperature T_∞ is below the boiling temperature T_{b}, and as the ambient water mole fraction when the ambient temperature is above the boiling point T_{b}.

As expected, increasing concentrations of liquid water in the droplet $\mathcal{V}$ rapidly delays autoignition, with τ_{ig} increasing nearly a 40% for $\mathcal{V} = 0.20$ respect to the anhydrous ethanol $\mathcal{V} = 0$. On the contrary, ambient humidity water mole concentration $\mathcal{H}$ slightly accelerates autoignition due to the extra heat released during moisture condensation.

The temporal evolution of the radial profiles of ethanol $Y_{\ell,\mathrm{EtOH}}$ and water $Y_{\ell,\mathrm{H_2O}}$ liquid mass fractions are plotted in Fig. B.7 together with their mass vaporisation rates, $\dot{m}_{\ell,\mathrm{EtOH}}$ and $\dot{m}_{\ell,\mathrm{H_2O}}$, for temperatures slightly above the critical autoignition temperature $T_\infty = 910K > T^c_\infty$ calculated for anhydrous ethanol droplets vaporizing in a dry ambient $\mathcal{V} = \mathcal{H} = 0$, as corresponds to the point indicated with a dot in Fig. B.4.

As shown in this figure, ethanol/water droplets completely vaporize without ignition at $T_\infty = 910$ K, mainly because the slower ethanol vaporization rate induced by the lower temperature reached at the droplet surface. Also, the smaller values of $\dot{m}_{\ell,\mathrm{EtOH}}$ contributed to slow down the convection of ethanol towards higher temperature regions, delaying the production of the radicals (H_2O_2 and HO_2) that would lead to autoignition.

The temporal evolution of $Y_{\ell,\mathrm{EtOH}}$ is plotted in Fig. B.7*b* at the time instants indicated in Fig. B.7*a*. The simultaneous evaporation of ethanol and water during most of the droplet lifetime keeps ethanol concentration gradients very small within the droplet. It is only when the droplet radius becomes very small that the diffusion of ethanol towards the droplet surface is hindered by the remaining water, inducing the large concentration gradients observed in the figure.

As shown in Fig. B.8, ambient moisture $\mathcal{H} \neq 0$ reduced ethanol droplet autoignition time. The extra heat released during the condensation of the atmospheric water vapor increased the droplet surface temperature when compared to that of dry air, accelerating ethanol vaporisation rates, as depicted in Fig. B.7*a* for $\mathcal{H} = 0.1$ and 0.2. The distribution of condensed water on the droplet, shown in Fig. B.7*d* at the time instants indicated in B.7*c*

for $\mathcal{H} = 0.2$, illustrates the formation of a boundary layer of liquid water on the droplet surface, that slowly diffuses towards the droplet center, mixing with the liquid ethanol. The distribution of the liquid water inside the droplet confirms the limitations of the rapid-mixing approximation, as shown in AppendixB, to properly predict ethanol vaporization rates and autoignition times in the presence of ambient moisture.

4. Conclusions

This numerical work analyzes the autoignition of ethanol droplets for a wide range of temperatures, taking into account both the water content of the liquid phase and the humidity of the hot atmosphere in which the droplet is initially located. The numerical description makes use of a 15-step, 17 species reduced mechanism [37] capable of accurately describing unsteady combustion phenomena of the type found during droplet autoignition.

The numerical simulation here presented predicted the autoignition time of ethanol droplets with different diameters and ambient conditions. In particular, the unsteady simulation starts describing the initial unsteady droplet evaporation and the simultaneous condensation of water on the droplet surface. After the autoignition event takes place, raising abruptly the temperature in a small region located relatively far from the droplet surface, the simulations detailed the formation of a lean premixed flame that propagates towards the droplet surface consuming all the available oxygen. After bouncing back, a travelling diffusion flame is formed that evolves slowly to reach a quasi-steady state when the stand-off distance r_f gradually increases as the droplet radius recedes.

Using our numerical results, we depicted a map that defines the critical ambient temperature T_∞^c below which autoignition can not take place for a droplet with initial diameter d_0. In ambient temperatures below T_∞^c, the droplet evaporates completely before the concentration of the hydroperoxil HO_2 and hydrogen peroxide radicals H_2O_2 are large enough to induce ignition. It was found that for small droplets ($d_0 < 50\mu$m) autoignition is ill-defined and, before it is complete, extinction takes place, even for high ambient temperatures.

In practical applications, liquid ethanol is commonly found with large quantities of dissolved water due to its large hygroscopic character [56]. To account for this effect, we analyzed water-ethanol droplets to find longer autoignition times and higher critical autoignition temperature as the water droplet content is increased, mainly due to the lower droplet surface temperature achieved for larger values of $X_{\ell,\mathrm{H_2O},0}$.

On the contrary, ethanol droplets autoignition becomes faster in humid ambiences as the water, coming either from the combustion products or from the ambient humidity, condensates and dissolve in the liquid ethanol forming a boundary layer that thickens with time. The extra heat released during the condensation of water accelerates the evaporation of the liq-

uid fuel, achieving autoignition conditions sooner than in dry atmospheres. Our calculations have shown that the assumption of rapid liquid-phase mixing is not sufficiently accurate when bi-component ethanol/water droplets are considered.

Acknowledgements

The authors want to express their gratitude to Professor Forman Williams in the conception and guidance of this work, in particular, and all the ongoing work on ethanol droplet vaporization and combustion. This work was supported by the projects ENE2015-65852-C2-1-R and PID2019-108592RB-C41 (MINECO/FEDER,UE).

[1] S. Sharma, S. K. Ghoshal, Hydrogen the future transportation fuel: from production to applications, Renewable and sustainable energy reviews 43 (2015) 1151–1158.

[2] F. A. Williams, Spray combustion and atomization, The Physics of Fluids 1 (6) (1958) 541–545.

[3] G. Faeth, Evaporation and combustion of sprays, Progress in Energy and Combustion Science 9 (1-2) (1983) 1–76.

[4] W. A. Sirignano, Fuel droplet vaporization and spray combustion theory, Progress in Energy and Combustion Science 9 (4) (1983) 291–322.

[5] H.-H. Chiu, Advances and challenges in droplet and spray combustion. i. toward a unified theory of droplet aerothermochemistry, Progress in Energy and Combustion Science 26 (4-6) (2000) 381–416.

[6] A. Williams, Combustion of droplets of liquid fuels: a review, Combustion and flame 21 (1) (1973) 1–31.

[7] A. Crespo, A. Liñán, Unsteady effects in droplet evaporation and combustion, Combustion Science and Technology 11 (1-2) (1975) 9–18.

[8] C. Law, H. Law, A d2-law for multicomponent droplet vaporization and combustion, AIAA journal 20 (4) (1982) 522–527.

[9] S. Sazhin, Droplets and sprays, Vol. 345, Springer, 2014.

[10] B. Guan, R. Zhan, H. Lin, Z. Huang, Review of state of the art technologies of selective catalytic reduction of nox from diesel engine exhaust, Applied Thermal Engineering 66 (1-2) (2014) 395–414.

[11] M. T. Javed, N. Irfan, B. Gibbs, Control of combustion-generated nitrogen oxides by selective non-catalytic reduction, Journal of environmental management 83 (3) (2007) 251–289.

[12] R. A. Stein, J. E. Anderson, T. J. Wallington, An overview of the effects of ethanol-gasoline blends on si engine performance, fuel efficiency, and emissions, SAE International Journal of Engines 6 (1) (2013) 470–487.

[13] M. Botero, Y. Huang, D. Zhu, A. Molina, C. K. Law, Synergistic combustion of droplets of ethanol, diesel and biodiesel mixtures, Fuel 94 (2012) 342–347.

[14] B.-Q. He, S.-J. Shuai, J.-X. Wang, H. He, The effect of ethanol blended diesel fuels on emissions from a diesel engine, Atmospheric Environment 37 (35) (2003) 4965–4971.

[15] G. M. Faeth, D. R. Olson, The ignition of hydrocarbon fuel droplets in air, SAE Transactions (1968) 1793–1802.

[16] T. Saitoh, S. Ishiguro, T. Niioka, An experimental study of droplet ignition characteristics near the ignitable limit, Combustion and Flame 48 (1982) 27–32.

[17] M. Takei, T. Tsukamoto, T. Niioka, Ignition of blended-fuel droplet in high-temperature atmosphere, Combustion and Flame 93 (1-2) (1993) 149–156.

[18] M. Tanabe, M. Kono, J. Sato, J. Koenig, C. Eigenbrod, F. Dinkelacker, H. Rath Zarm, Two stage ignition of n-heptane isolated droplets, Combustion Science and technology 108 (1-3) (1995) 103–119.

[19] I. Javed, S. W. Baek, K. Waheed, Autoignition and combustion characteristics of heptane droplets with the addition of aluminium nanoparticles at elevated temperatures, Combustion and Flame 162 (1) (2015) 191–206.

[20] W. Han, B. Dai, J. Liu, Y. Sun, B. Zhu, X. Liu, Ignition and combustion characteristics of heptane-based nanofluid fuel droplets, Energy & Fuels.

[21] R. Stauch, S. Lipp, U. Maas, Detailed numerical simulations of the autoignition of single n-heptane droplets in air, Combustion and flame 145 (3) (2006) 533–542.

[22] V. Y. Basevich, A. Belyaev, S. Medvedev, V. Posvyanskii, F. Frolov, S. Frolov, Simulation of the autoignition and combustion of n-heptane droplets using a detailed kinetic mechanism, Russian Journal of Physical Chemistry B 4 (6) (2010) 995–1004.

[23] A. Cuoci, A. Frassoldati, T. Faravelli, E. Ranzi, Numerical modeling of auto-ignition of isolated fuel droplets in microgravity, Proceedings of the Combustion Institute 35 (2) (2015) 1621–1627.

[24] A. Lee, C. K. Law, An experimental investigation on the vaporization and combustion of methanol and ethanol droplets, Combustion Science and Technology 86 (1-6) (1992) 253–265.

[25] S. B. Saharin, B. Lefort, C. Morin, C. Chauveau, L. Le Moyne, R. Kafafy, Vaporization characteristics of ethanol and 1-propanol droplets at high temperatures, Atomization and Sprays 22 (3).

[26] S. Kotake, T. Okazaki, Evaporation and combustion of a fuel droplet, International Journal of Heat and Mass Transfer 12 (5) (1969) 595–609.

[27] H. Hara, S. Kumagai, Experimental investigation of free droplet combustion under microgravity 23 (1) (1991) 1605–1610.

[28] A. Yozgatligil, S.-H. Park, M. Y. Choi, A. Kazakov, F. L. Dryer, Influence of oxygen concentration on the sooting behavior of ethanol droplet flames in microgravity conditions, Proceedings of the Combustion Institute 31 (2) (2007) 2165–2173.

[29] Á. Muelas, P. Remacha, J. Ballester, Combustion characteristics of isolated free-falling droplets of jet a blended with ethanol and butanol, in: ASME Turbo Expo 2018: Turbomachinery Technical Conference and Exposition, American Society of Mechanical Engineers Digital Collection, 2018.

[30] H. Li, C. D. Rosebrock, N. Riefler, T. Wriedt, L. Mädler, Experimental investigations on the effects of water vapor and oxygen concentrations in the ambience on the burning constant, lifetime and residuals of single isolated xylene, isobutanol and ethanol droplets, Experimental Thermal and Fluid Science (2019) 109920.

[31] A. Kazakov, J. Conley, F. L. Dryer, Detailed modeling of an isolated, ethanol droplet combustion under microgravity conditions, Combustion and Flame 134 (4) (2003) 301–314.

[32] M. Mehl, A. Cuoci, T. Faravelli, E. Ranzi, A. Kazakov, F. L. Dryer, A. Yozgatligil, S.-H. Park, M. Y. Choi, Combustion of ethanol fuel droplets in microgravity conditions, in: Proceedings of the 20th ILASS-Europe Meeting, page Invited paper, Orleans, France, 2005.

[33] A. J. Marchese, F. L. Dryer, The effect of liquid mass transport on the combustion and extinction of bicomponent droplets of methanol and water, Combustion and Flame 105 (1-2) (1996) 104–122.

[34] A. Millán-Merino, E. Fernández-Tarrazo, M. Sánchez-Sanz, F. A. Williams, A multi-purpose reduced mechanism for ethanol combustion, Combustion and Flame 193 (2018) 112–122.

[35] A. Millán-Merino, E. Fernández-Tarrazo, M. Sánchez-Sanz, F. A. Williams, Modified multi-purpose reduced chemistry for ethanol combustion, Submitted to Combustion and Flame.

[36] Fluid Mechanics Group web page (Combustion Research), (http://fluidosuc3m.es/research/combustion/downloads) Universidad Carlos III de Madrid, version 2017-12-20.

[37] A. Millán-Merino, E. Fernández-Tarrazo, M. Sánchez-Sanz, F. A. Williams, Modified multipurpose reduced chemistry for ethanol combustion, Combustion and Flame 215 (2020) 221–223.

[38] R. J. Kee, J. Warnatz, J. A. Miller, Fortran computer-code package for the evaluation of gas-phase viscosities, conductivities, and diffusion coefficients.[chemkin], Tech. rep., Sandia National Labs., Livermore, CA (USA) (1983).

[39] T. Coffee, J. Heimerl, Transport algorithms for premixed, laminar steady-state flames, Combustion and Flame 43 (1981) 273–289.

[40] C. Wilke, P. Chang, Correlation of diffusion coefficients in dilute solutions, AIChE Journal 1 (2) (1955) 264–270.

[41] M. Aalto, K. I. Keskinen, J. Aittamaa, S. Liukkonen, An improved correlation for compressed liquid densities of hydrocarbons. part 2. mixtures, Fluid phase equilibria 114 (1-2) (1996) 21–35.

[42] P. Kadlec, S. Henke, Z. Bubnik, et al., Properties of ethanol and ethanol-water solutions-tables and equations., Sugar Industry/Zuckerindustrie 135 (10) (2010) 607–613.

[43] Water - Density, Specific Weight and Thermal Expansion Coefficient, `https://www.engineeringtoolbox.com/water-density-specific-weight-d_595.html`, last access (January 2019).

[44] R. A. Svehla, Transport coefficients for the NASA Lewis chemical equilibrium program, NASA Lewis Research Center, Technical Memorandum 4647.

[45] Chemical-Kinetic Mechanisms for Combustion Applications, web.eng.ucsd.edu/mae/groups/combustion/mechanism.html, v. 2016-12-14.

[46] E. Goos, A. Burcat, B. Ruscic, Extended third millennium ideal gas and condensed phase thermochemical database for combustion with updates from active thermochemical tables, Elke Goos, Remchingen, Germany, accessed Sept 19 (2010) 2016.

[47] J. Hirschfelder, C. F. Curtiss, R. Bird, The Molecular Theory of Gases and Liquids, John Wiley & Sons, 1964.

[48] S. Mathur, P. Tondon, S. Saxena, Thermal conductivity of binary, ternary and quaternary mixtures of rare gases, Molecular physics 12 (6) (1967) 569–579.

[49] L. Filippov, Vest. mosk. univ., ser. fiz. mat. estestv, Nauk 8 (1955) 67–69.

[50] L. Grunberg, A. H. Nissan, Mixture law for viscosity, Nature 164 (4175) (1949) 799.

[51] M. Criado-Sancho, J. Casas-Vázquez, Termodinámica química y de los procesos irreversibles, no. 541.369 C7, 1997.

[52] A. Fredenslund, J. Gmehling, P. Rasmussen, Vapor-liquid Equilibria Using UNIFAC: A Group-contribution Methods, Elsevier Scientific, 1977.

[53] S. S. Sazhin, Advanced models of fuel droplet heating and evaporation, Progress in energy and combustion science 32 (2) (2006) 162–214.

[54] A. Liñán, F. A. Williams, Fundamental aspects of combustion, New York, NY (United States); Oxford University Press, 1993.

[55] A. Linan, et al., The asymptotic structure of counterflow diffusion flames for large activation energies, Acta Astronautica 1 (7-8) (1974) 1007–1039.

[56] R. J. Brown, A. C. Keates, A. S. Brown, Optimised determinations of water in ethanol by encoded photometric near-infrared spectroscopy: A special case of sequential standard addition calibration, Analytica chimica acta 690 (1) (2011) 47–52.

[57] V. Shamanskii, A modification of newton's method, Ukrainian Mathematical Journal 19 (1) (1967) 118–122.

[58] C. Diddens, Detailed finite element method modeling of evaporating multi-component droplets, Journal of Computational Physics 340 (2017) 670–687.

[59] C. K. Law, Recent advances in droplet vaporization and combustion, Progress in energy and combustion science 8 (3) (1982) 171–201.

[60] C. Law, Unsteady droplet combustion with droplet heating, Combustion and Flame 26 (1976) 17–22.

[61] B. Zhang, F. Williams, Alcohol droplet combustion, Acta Astronautica 39 (8) (1996) 599–603.

AppendixA. Numerical method

We will give here a brief description of the numerical method used to solve the mathematical problem. The set of equations (1)-(3) are discretized using a second-order, finite volume discretization for the spatial derivatives and a first-order backward Euler discretization for the temporal derivatives. The maximum time step Δt is limited by the sudden autoignition event, that required a very small $\Delta t < 10^{-4}$s to be properly described, canceling the advantages regarding the use of larger time steps that an implicit or high-order temporal discretization might introduce. A non-uniform grid with typically 120 points is used to discretize a fluid domain that spans $300a_0$, with a maximum clustering of points at the gas-liquid interface where the maximum gradients are located. The minimum and maximum grid steps are $\Delta r/a_0 = 0.05$ and $\Delta r/a_0 = 12$, respectively.

The set of discretized equations (1)-(3) together with the boundary (13)-(17) and initial conditions (22) are solved in a spherical domain using a modified Newton-Raphson method that minimizes an error function f formed substracting the left and right hand side terms of the equations. At a generic time t, the iterative procedure starts $k = 0$ using the value of the variables ψ (liquid and gas phase velocities and densities, temperature, droplet radius and species concentrations) at the previous time step $\psi^{k=0}(t) = \psi(t - \Delta t)$. During the iteration, the value of the variables is updated according to $\psi^{k+1}(t) = \psi^k(t) - \lambda J^{-1} f^k$, with $\lambda < 1$ being a damping parameter. To speed up the calculations, the Jacobian matrix J is recalculated every 20 iterations [57]. The iteration procedure continues until the ∞-norm of the error function satisfies $\left|f^k\right|_\infty < 10^{-8}$. Typically, around $k = 200$ iterations per time step are needed to achieve convergence.

To track the position of the gas-liquid interface we implemented a moving mesh method [58] that used a two-steps, predictor-corrector strategy. Once the new value of the variables are known, we computed the new position of the interface $\dot{a} = \dot{m}''/\rho_\ell + (u_\ell)_{r=a}$ and the location

Property Name	**Symbol**	**Property Value**
Molecular Weight	W	46.07 g/mol
Boiling Temperature	T_{b}	351.4 K
AdiabaticTemperature	T_{ad}	2217 K
Ethanol Density	$\rho_{\ell}(T_{\mathrm{b}})$	738.8 kg/m^3
Heat of Vaporization	$\mathrm{L_b}(T_{\mathrm{b}})$	850.8 kJ/kg
Thermal Conductivity	$k_{\mathrm{g}}^{\mathrm{air}}(T_{\mathrm{m}})$	0.082 W/m K

Table B.1: Physical properties of ethanol

of the grid points that conformed the new mesh using the recession velocity $v_s = r\dot{a}/a(t)$. The value of the variables ϕ are recalculated in the new grid and the procedure continues until the normalized difference between the interface position calculated in two consecutive iterations falls below 10^{-5} .

AppendixB. Model validation: Quasi-steady droplet combustion

In the quasi-steady combustion of an isolated droplet, the diffusion rate controls the combustion process and the net mass fuel flux vaporized from the droplet is consumed in the flame region [59]. Even though, in this regime, the time derivatives in eqns. (1)-(17) are negligible, the results shown below were obtained using the fully unsteady formulation given above.

To experimentally achieve quasi-steady conditions early in the droplet life time, the ignition process is forced, in this validation case, by an external energy source, avoiding the initial vaporization and auto-ignition stages to maximize the observation time [24].

The physical models and numerical code described above in appendix A are validated in Fig. B.9 by comparing our numerical results with the experimental measurements by Lee and Law [24] for the combustion of an ethanol droplet with initial diameter $d_0 = 0.226$ mm in a hot and humid atmosphere formed by the products of a lean CH_4-O_2-N_2 premixed flame. The initial conditions (20)-(21) are replaced by the steady solution of the equations (1)-(19), achieved for the composition and temperature of this specific atmosphere. Also, in the same figure, we compared our computations with the numerical results obtained by Kazakov et al. in [31]. As can be seen in Fig. B.9, our results show an excellent agreement in droplet size history and only minor differences are observed in the prediction of the water concentration in the liquid phase (Fig. B.9*b*). Kazakov and Drier [31] improved the numerical prediction of $Y_{\mathrm{H_2O}}$ in the droplet by empirically adjusting the effective diffusion coefficient of liquid water in ethanol.

AppendixB.1. The validity of the Well-Mixed-Liquid approximation

During the combustion of alcohol droplets, water vapor, either from the ambience or generated at the flame, can condense at the droplet surface and dissolve into the droplet interior [24]. The heat release associated to the condensation and dilution of the droplet alcohol concentration, alters the vaporization rate and cannot be neglected. The model described above takes into account this effect, as has been demonstrated in Fig. B.9. Nevertheless, as a simpler alternative, several numerical studies described the droplet combustion by applying the Well-Mixed-Liquid (WML) approximation [33, 60] in which the droplet temperature and composition can be considered homogeneous. Formally, this limit is valid in the limit in which the liquid phase homogenization time $a_0^2/D_{T,\ell}$ is much shorter than the droplet lifetime $t_{\rm evap} \sim (4\pi a_0^3 \rho_\ell/3)/(4\pi a_0^2 \dot{m}'')$, and the droplet becomes a well-mixed, uniform control volume for which the liquid phase equations (2) and (3) reduce to

$$\frac{\mathrm{d}}{\mathrm{d}t}(\rho_\ell Y_{\ell,i} V_d) = (\dot{m}''(Y_{\mathrm{g},i})_{r=a} - (J_{\mathrm{g},i})_{r=a}) A_d, \quad i = 1, ..., N_\ell;\ i \neq I \tag{B.1}$$

$$\frac{\mathrm{d}}{\mathrm{d}t}(\rho_\ell h_\ell V_d) = (\dot{m}''(h_{\mathrm{g}})_{r=a} - (q_{\mathrm{g}})_{r=a}) A_d \tag{B.2}$$

where V_d and A_d are, respectively, the droplet volume and surface area at time t. The results using this limit are also included in Fig. B.9 and, as can be easily checked, the results do not match with the experimental measurements or with the numerical calculations that take into account the diffusion in the liquid phase. According to our results, the Well-Mixed-Liquid model overestimates the condensation of water on the droplet surface. Additionally, and contrary to methanol droplets [61], the diffusion of water in the liquid phase is small, inducing the formation of a boundary layer of condensed water that soon begins vaporizing along with the fuel. Contradicting the assumptions behind the well-mixed liquid hypothesis, both temperature and concentration are not homogeneous inside the fuel droplet.

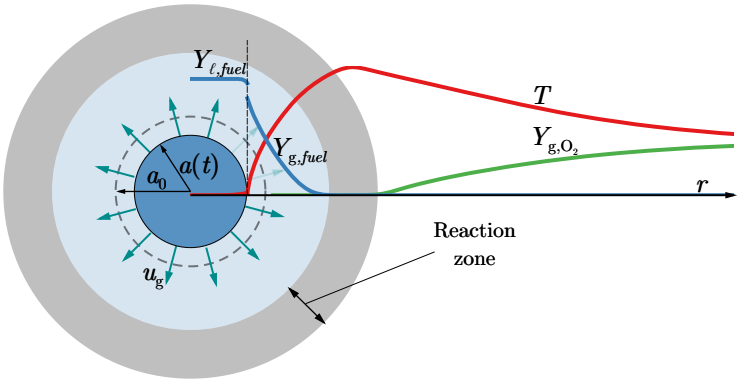

Figure B.1: Sketch of the spherically-symmetrical droplet vaporization and combustion problem.

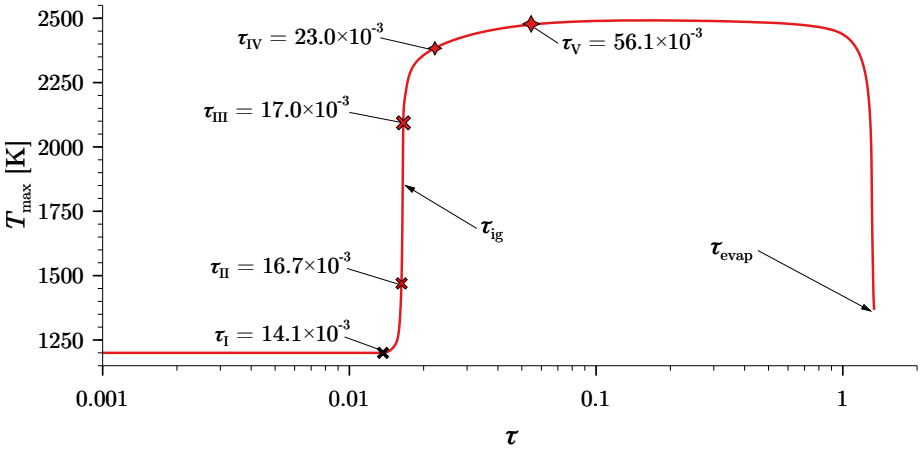

Figure B.2: Autoignition of ethanol-air droplets of $d_0 = 1$mm and $T_{d_0} = 300$K at ambient temperature $T_\infty = 1200$K. Solid line represents the maximum gas temperature as function of non-dimensional time, symbols represent selected times for the profiles shown in Fig. B.3. Simulations for droplet autoignition at were conducted using a multipurpose 15-steps reduced mechanism for ethanol combustion developed in [34].

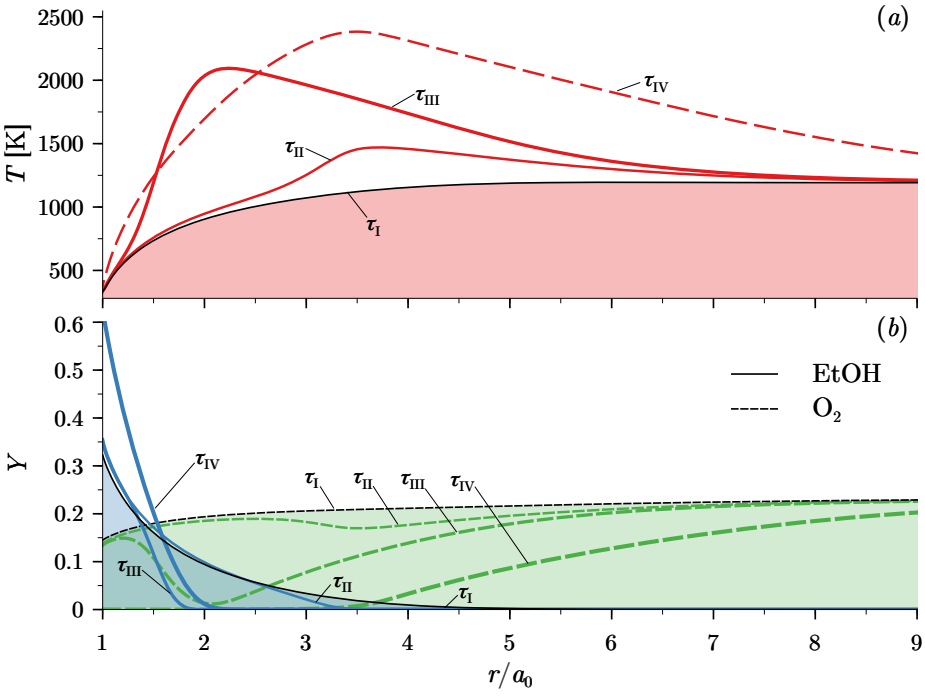

Figure B.3: Autoignition ethanol droplets in air atmosphere with same conditions as described in Fig. B.2. **Subfigure (*a*)**: Temperature profiles as function of normalized distances in different instants. **Subfigure (*b*)**: Mass fraction profiles as function of normalized distances. Solid lines represents mass fraction profiles of ethanol and dashed lines are oxygen mass fraction. Time moments corresponds with figure B.2.

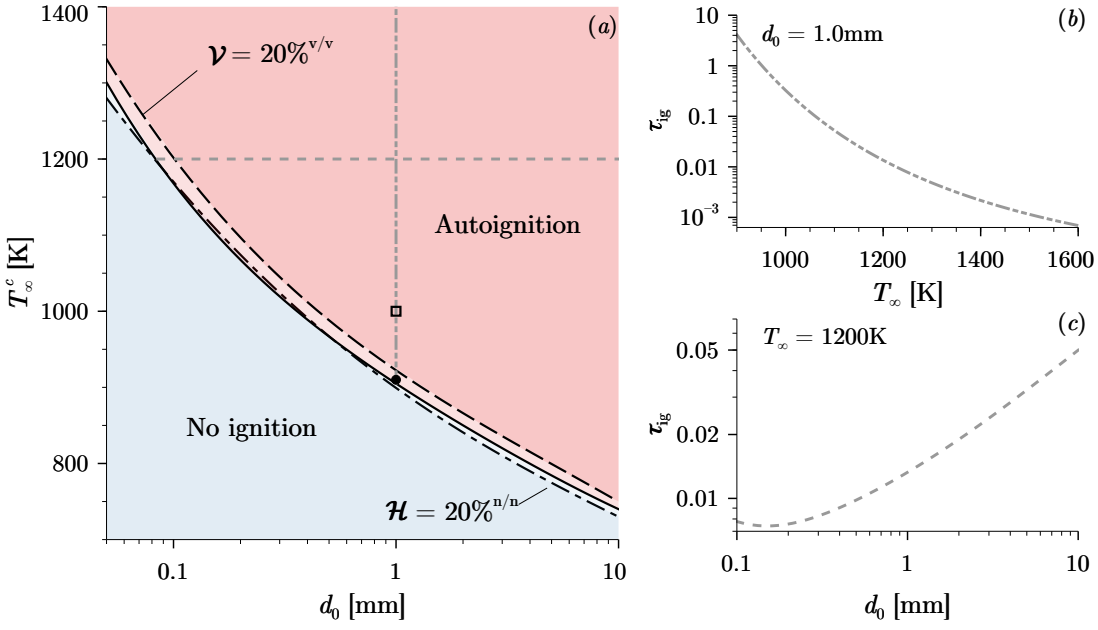

Figure B.4: **Subfigure (*a*)**: Critical temperature for autoignition T_∞^c as a function of the initial droplet diameter d_0 for ethanol-air droplets of $T_{d_0} = 300$K at atmospheric pressure. Solid line represent case without water (droplet or ambient content) dashed lines represent the effect of water droplet content and dash-doted lines represent the effect of ambient water mole fraction. The dot and the square included in the Figure indicate the point $d_0 = 1$ mm and $T_\infty = (910, 1000)$ k, respectively, analyzed in detail in Figs. B.7 and Fig. B.8. **Subfigure (*b*)**: Droplet autoignition time, $\tau_{ig} = t_{ig}/t_{evap}$, as function of ambient temperature T_∞ for $d_0 = 1$mm. **Subfigure (*c*)**: Droplet autoignition time as function of initial diameter for $T_\infty = 1200$K; where time scale, t_{evap}, is calculated for $d_0 = 1$mm.

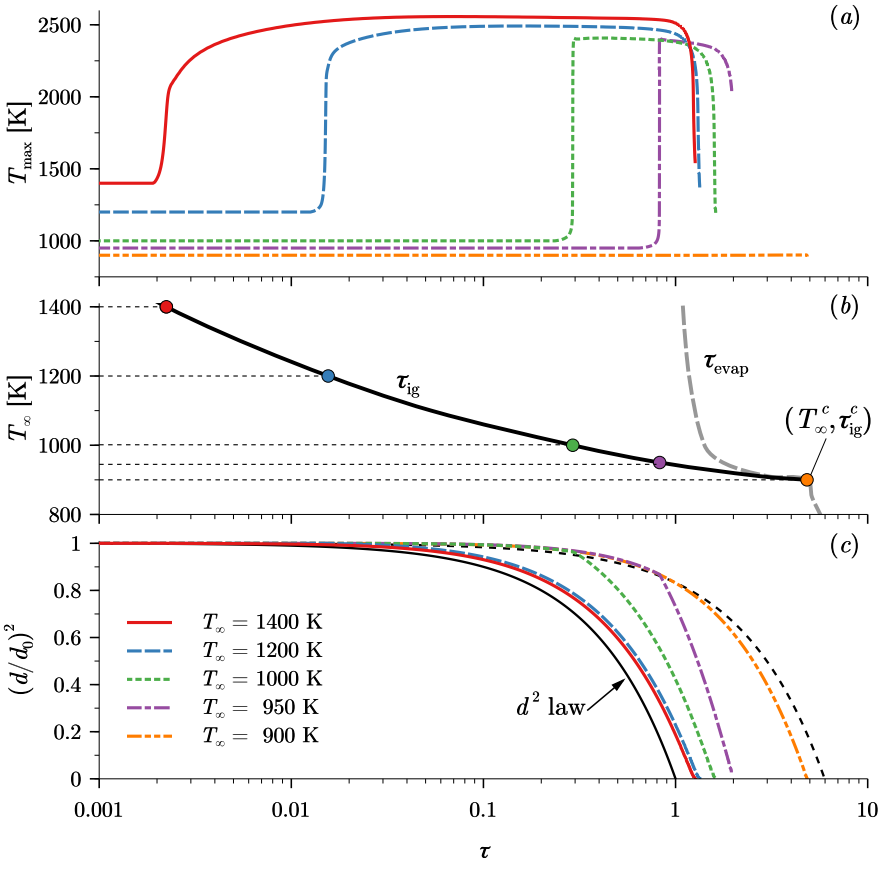

Figure B.5: Ignition of an isolated droplet of ethanol with initial temperature $T_{d_0} = 300$K and diameter $d_0 = 1$mm in hot air at pressure $p_\infty = 1$atm and temperature T_∞ (indicated in the figure). **Subfigure (*a*)**: Time evolution of the maximum temperature in the gas phase. **Subfigure (*b*)**: Droplet autoignition and evaporation times as function of ambient gas temperature. **Subfigure (*c*)**: Droplet normalized surface (d^2/d_0^2) as function of non-dimensional time τ. The solid black line depicts the d^2-law such that $d^2/d_0^2 = 1-\tau$ and the dotted black line represents the pure vaporization d^2-law as estimated from Eq. (23) for ambient gas temperature $T_g = 900$K.

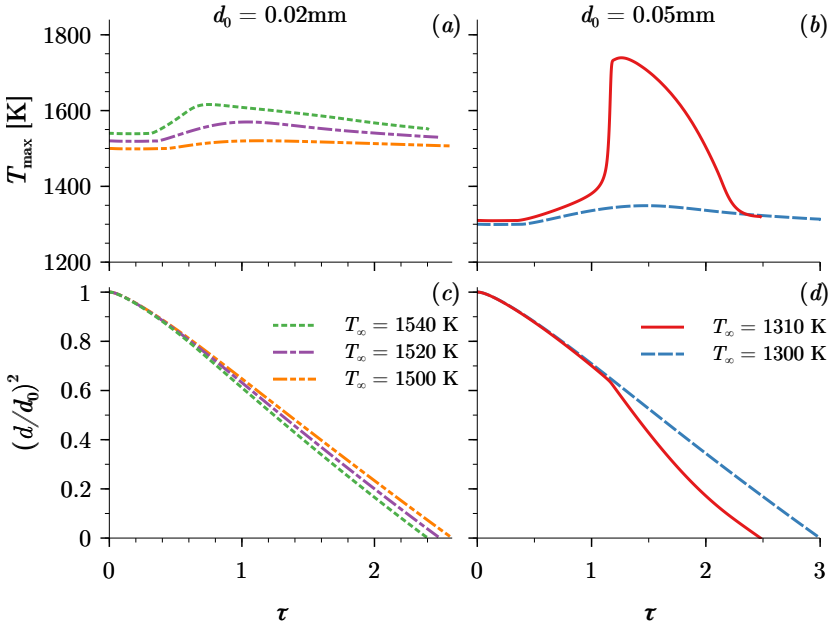

Figure B.6: Ignition of an isolated droplet of ethanol with initial temperature $T_{d_0} = 300$K in hot air at pressure $p_\infty = 1$atm and temperature T_∞ (indicated in the figure). **Subfigure (*a*&*b*)**: Time evolution of the maximum temperature in the gas phase for initial diameters $d_0 = 0.02$ and 0.05mm respectively. **Subfigure (*c*&*d*)**: Droplet normalized surface (d^2/d_0^2) as function of non-dimensional time τ for $d_0 = 0.02$ and 0.05mm respectively.

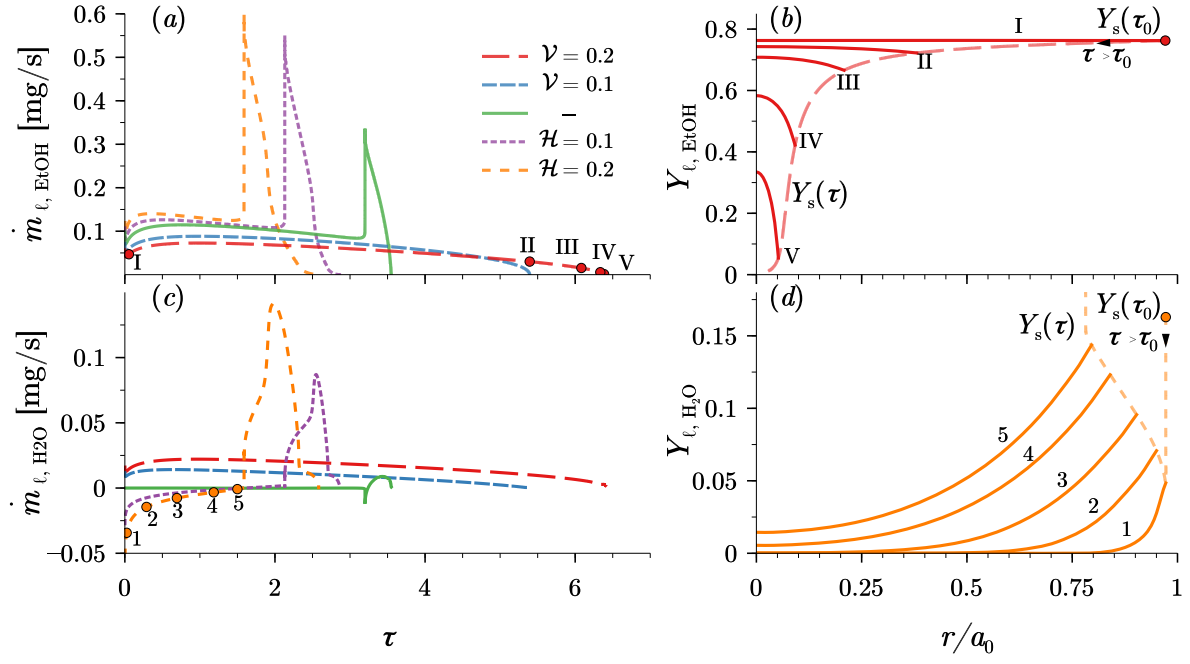

Figure B.7: Effect of the water droplet content $X_{l,H_2O,0}$ and ambient water mole fraction $X_{g,H_2O,\infty}$ on the ignition of an isolated droplet of ethanol with initial temperature $T_{d_0} = 300$K and diameter $d_0 = 1$mm in hot air at pressure $p_\infty = 1$atm and temperature $T_\infty = 910$K. **Subfigure (*a*)**: Time evolution of ethanol mass evaporation rate $\dot{m}_{l,\mathrm{EtOH}}$. **Subfigure (*b*)**: Radial distribution of liquid ethanol inside a droplet with water content $20\%^{v/v}$ at the time instants indicated in subfigure (a). **Subfigure (*c*)**: Time evolution of liquid water mass evaporation rate $\dot{m}_{l,\mathrm{H_2O}}$. **Subfigure (*d*)**: Radial distribution of liquid water inside a droplet vaporising in an ambient with $20\%^{v/v}$ relative humidity at the times indicated in subfigure (c).

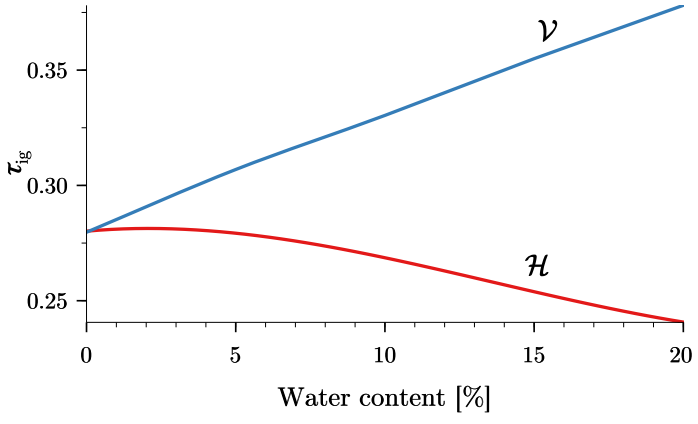

Figure B.8: Autoignition time for ethanol-air droplets versus initial water content, $\mathcal{V}$, and ambient water mole fraction, $\mathcal{H}$, for initial droplet diameter $d_0 = 1$mm at ambient temperature $T_\infty = 1000$K and oxygen at mole concentration 21%.

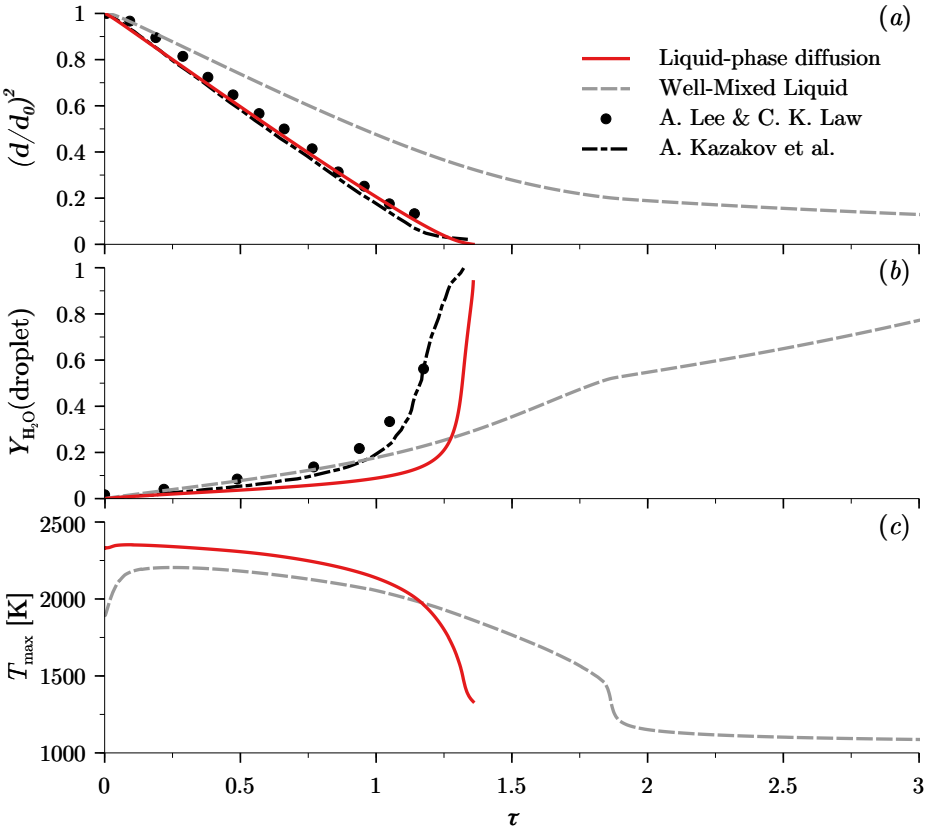

Figure B.9: Ethanol droplet combustion in a hot atmosphere formed with the gas products of a premixed CH_4-O_2-N_2 flame [24]. **Subfigure (*a*)**: Droplet normalized surface $(d/d_0)^2$ as function of non-dimensional time $\tilde{\tau} = t/\tilde{t}_{\text{evap}}$, with $\tilde{t}_{\text{evap}}$ the evaporation time defined in eq. (23). **Subfigure (*b*)**: Droplet average water mass fraction against time. **Subfigure (*c*)**: Maximum gas temperature versus time. Symbols: experimental results of [24]; black dash-dot line: numerical results of [31]; red solid line: present work, including liquid-phase diffusion ; grey dashed line: present work with Well-Mixed-Liquid (WML) model